Copyright WILEY-VCH Verlag GmbH & Co. KGaA, 69469 Weinheim, Germany, 2016.

ADVANCED
ELECTRONIC
MATERIALS

Supporting Information

for *Adv. Electron. Mater.,* DOI: 10.1002/aelm.201600470

Influence of Interface Morphology on Hysteresis in Vapor-Deposited Perovskite Solar Cells

*Jay B. Patel, Jennifer Wong-Leung, Stephan Van Reenen, Nobuya Sakai, Jacob Tse Wei Wang, Elizabeth S. Parrott, Mingzhen Liu, Henry J. Snaith, Laura M. Herz, and Michael B. Johnston**

Submitted to ADVANCED MATERIALS

DOI: 10.1002/aelm.201600470

Influence of interface morphology on hysteresis in vapour deposited perovskite solar cells.

By *Jay B. Patel, Jennifer Wong-Leung, Stephan Van Reenen, Nobuya Sakai, Jacob Tse Wei Wang, Elizabeth S. Parrott, Mingzhen Liu, Henry J. Snaith, Laura M. Herz, Michael B. Johnston**

[*]Michael B Johnston
Department of Physics
University of Oxford
Clarendon Laboratory
Parks Road
Oxford OX1 3PU
E-mail: michael.johnston@physics.ox.ac.uk

Supporting Information

Contents

Experimental techniques Page 2

All device schematics and combined Statistics ***(Figure S1)*** Page 7

Device characteristics Relating to Figure 1 ***(Table S1)*** Page 7

Comparison of Type B (regular) and Type D (inverted) devices ***(Figure S2)*** Page 8

Using Spiro-OMeTAD in an inverted device (Type F) ***(Figure S2c)*** Page 8

Additional TEM Images and EDS Maps ***(Figure S3)*** Page 9

Thermal Admittance Spectroscopy (TAS) ***(Figure S4a)*** Page 10

Photoluminescence Transient plots (PL) ***(Figure S4c)*** Page 10

Device characteristics Relating to Figure 2 ***(Table S2)*** Page 11

External Quantum Efficiency Measurements ***(Figure S5)*** Page 11

TAS Mott-Schottky plots ***(Figure S6 & S7)*** Page 12

Further SEM images to Figure 3 ***(Figure S8)*** Page 14

Absorbance ***(Figure S9)*** Page 16

X-ray Diffraction Pattern ***(Figure S10)*** Page 16

Experimental techniques

Fabrication of Devices

All materials were bought from Sigma Aldrich, unless stated otherwise.

Cleaning of substrate:

Fluorine doped tin Oxide (Pilkington) substrates were cleaned with hallmanex (%) solution, followed by a rinse with distilled water. The substrate was then twice washed with Acetone, Isopropanol, and Ethanol. Thereafter the substrates were plasma etched in O_2 for 10minutes.

Type A

TiO_2 was prepared as reported previously[20]. Briefly titanium isopropoxide is dissolved in anhydrous ethanol solution followed by a proportional addition of 0.02mol HCl. The solution was then spin coated on the FTO substrate at 2000rpm for 45 seconds. This was followed by a high temperature sintering (500°C) for 45minutes. $MAPbI_3$ was deposited by thermal co-evaporation (see below). The films were annealed at 100°C for 60 minutes (No annealing for Batch study). Thereafter spiro-OMeTAD was dissolved in chlorobenzene (8%wt) with added tert-butylpiridine (tBP) and lithium bis(trifluoromethanesulfonyl)imide (Li-TFSI). The solution was spin coated at 2000rpm for 45 seconds.

Type B

C_{60} was spin coated as reported previously[30]. Briefly C_{60} (Solenne b.v. 99.5%) was dissolved in 1,2-dichlorobenzene (DCB), 10mg/ml, and then spin coated at 1500rpm. After drying for 2 minutes at 55°C the substrates were taken into the glovebox. $MAPbI_3$ was deposited by thermal co-evaporation (see below) The films were annealed at 100°C for 15minutes. Thereafter spiro-OMeTAD deposited as mention above.

Type C

$TiCl_4$ solution was prepared as reported previously.[36] PCBM (Solenne b.v. 99.5%) was dissolved in DCB in either a 7.5mg/ml or 15mg/ml solution to get a 50nm or 100nm thickness respectively. The solution was then spin coated at 2000rpm for 45 seconds. $MAPbI_3$ was deposited by thermal co-evaporation (see below). The films were annealed at 100°C for 15minutes (No annealing for Batch study). Thereafter spiro-OMeTAD deposited as mention above.

Type D

F4-TCNQ doped Poly TPD (1-material) was spin coated at 2000rpm for 45seconds.[27] The samples were heated for 10minutes at 100°C. $MAPbI_3$ was deposited by thermal co-evaporation (see below). The films were then annealed for 60 minutes at 100°C. PCBM dissolved in DCB, 10mg/ml, followed by spin coating at 1000rpm. The substrates were heated for 10minutes at 100°C. A thin buffer layer of bathocuproine (BCP) dissolved in isopropanol was spin coated at 6000 rpm.

Type E

PCBM (Solenne b.v 99.5%) was dissolved in DCB in a 7.5mg/ml solution to get a 50nm thickness. The solution was then spin coated at 2000rpm for 45 seconds. $MAPbI_3$ was deposited by thermal co-evaporation (see below). The films were annealed at 100°C for 15minutes (No annealing for Batch study). Thereafter spiro-OMeTAD deposited as mention above.

Type F

spiro-OMeTAD was dissolved in chlorobenzene (8%wt) with added tBP and Li-TFSI and spin coated at 2000rpm for 45seconds. $MAPbI_3$ was deposited by thermal co-evaporation (see below). The films were then annealed for 60minutes at 100°C PCBM dissolved in DCB, 10mg/ml, followed by spin coating at 1000rpm. The substrates were heated for 10minutes at 100°C. A thin buffer layer of bathcuproine (BCP) dissolved in isopropanol was spin coated at 6000rpm.

Thermal Co-evaporation of $CH_3NH_3PbI_3$ ($MAPbI_3$).

The tooling factor was determined by depositing the starting powders, PbI_2 and methylammonium iodide (MAI), separately and then measuring the layer thicknesses using the DEKTAK surface profilometer. MAI was purchased from Oxford Photovoltaics and Lead(II) iodide, ultra-dry 99.999% (metals basis), was purchased from Alfa Aesar.

MAI and PbI_2 (500mg of each) were placed in separate crucibles, and the substrates were mounted on a rotating substrate holder to ensure that a uniform film was deposited. The temperature of the substrates was kept at 21 °C throughout the deposition. The chamber was allowed to reach a high vacuum (10^{-6} mbar), before heating the PbI_2 and the MAI crucibles to reach a rate of 0.4Ås^{-1}. Once the deposition rate had stabilized along with the pressure ($3x10^{-6}$mbar), the substrates were exposed to the vapour. The rates of both the MAI and PbI_2 were monitored using a quartz crystal microbalance to ensure a 1:1 molar ratio was achieved in the final composition of the film. The final deposition rate was 0.8 Å s^{-1}, and the thickness of the films was 300 nm (DEKTAK 150 profiler). Note, the excess materials left in the crucible could be used multiple times until finished. Furthermore, QCM sensors needed to be changed every 3-4 depositions.

Evaporation of Metal contacts

70nm Silver contacts were thermally evaporated with a shadow mask. The base pressure was allowed to reach 10^{-6}mbar before initiating the evaporation. For the Thermal Admittance Spectroscopy, the devices had a 50nm gold contact evaporated in a similar way.

Current Voltage Characterization

The solar cells were measured under simulated AM1.5, 100mW cm^{-2} sunlight (1sun), ABET Technologies Sun 2000, and a Keithly 2400 Sourcemeter in ambient conditions. Calibration of the lamp was with a NREL-calibrated KG5 Filtered Silicon reference. The active area of each device was defined by a mask which exposed a 0.0919cm^2 active area for testing of both the current voltage measurements and the stabilized power measure measurements. The Scan rate was 0.38Vs^{-1} for both the reverse and forwards sweep for all the devices

measured. The devices were kept at the voltage defined at maximum power, which was determined from the JV scans, for 50 seconds to measure the SPO and current density. Devices that had less than 1 $mAcm^{-2}$ were deemed non-working.

Scanning electron microscopy.

Images were taken using a Hitachi S-4300 microscope.

Thermal Admittance Spectroscopy

Thermal admittance spectroscopy (TAS) was carried out using an Autolab impedance spectrometer at frequencies between 0.1 Hz to 1 MHz. The samples were mounted in an Oxford Instruments optistat where the temperature of the sample could be controlled in vacuum.[37,38] The contact area used for the measurements was approximately 0.01 cm^2

Photoluminescence transients

Photoluminescence (PL) decay traces were acquired using a time-correlated single photon counting (TCSPC) setup. Samples were stored in a nitrogen glove box, and measured in ambient air. They were excited at 398 nm with an electronically triggered pulsed diode laser (PicoHarp LDH-D-C-405M) from the perovskite side of the film at a repetition rate of 5 MHz and a power of 140 μW. (fluence of 156 nJ cm^{-2}) Photoluminescence was collected and focused onto a grating spectrometer (Princeton Instruments, SP-2558) and detected at 765nm using a silicon single photon avalanche diode, acquiring for 30 minutes.

External Quantum Efficiency measurements.

External quantum efficiency (EQE) was measured via custom build Fourier transform photocurrent spectrometer based on a Bruker Vertex 80v Fourier Transform Interferometer. Devices were illuminated with simulated sunlight (AM 1.5 Sunlight, ~100 mW cm^{-2}). Devices were calibrated to a Newport-calibrated reference silicon solar cell with a known external quantum efficiency. The solar cells were masked with the same metal aperture as the ones used for the current voltage characterization, with a defined active area, 0.0919 cm^2.

***Visible absorption spectroscopy*.**

Transmission and reflection measurements were taken using a Bruker Vertex 80v Fourier Transform Interferometer with a silicon diode detector and a tungsten halogen light source.

***X-ray diffraction Measurements*.**

2θ measurements were performed using an X-ray diffractometer (Panalytical X'Pert Pro). The scan speed was 0.02 °/s for 30 minutes (Cu-Kα radiation operating at 40 kV and 40 mA). The diffraction patterns were corrected against tilt using quartz as a reference peak (2θ=16.43°).

Transmission Electron Microscopy (TEM)

TEM samples of the devices were prepared by focused ion beam (FIB) using a Ga beam in a FEI Helios 600 NanoLab instrument. These samples were transferred onto a TEM carbon grid. TEM analysis was carried out in a JEOL2100F instrument operated at 200 keV and equipped with STEM capabilities and a silicon drift detector for EDX analysis. We note that the sparse C intensity throughout the images are a result of the C grid used as support for the TEM sample.

Focussed Ion Bean (FIB) Milling

TEM samples of the devices were prepared by focused ion beam (FIB) using a Ga beam in a FEI Helios 600 NanoLab instrument. Firstly, Pt was deposited on the regions of interest to protect the specimen during the milling process. The coarse milling/cutting process was carried out with an initial 30keV Ga beam to slice a trapezoid-shaped sample and the sample thinned to 800 nm with a 30keV Ga beam. Further thinning/milling process was carried out with gradually lower ion beam current at each step with the milling performed on both sides of the specimen at each step to reduce re-deposition of sputtered materials.[39] A fine thinning process was then carried out using a 16keV voltage and 45pA current to thin the TEM lamella to less than 100nm for electron transparency. The final cleaning process was performed with a lower accelerating voltage 5 keV and 16 pA current so as to reduce the level of Ga implantation dramatically.[40] The sample slice was lifted out with a glass micromanipulator and mounted on the TEM carbon grid. All the samples were prepared with the same procedure.

While FIB can generate amorphous regions, we believe that the low energy (5keV) Ga beam (with an incident angle of 52°) used for the cleaning process will remove all the amorphous regions created by the FIB process. A simulation of the Ga collision (www.srim.org) within $MAPbI_3$ assuming a density of 4.16 g/cm^3 shows that the projected range of the ion is around 8nm and is an estimate of the expected amorphous layer produced for 5 keV Ga beam in a $MAPbI_3$ crystal.

All device architectures.

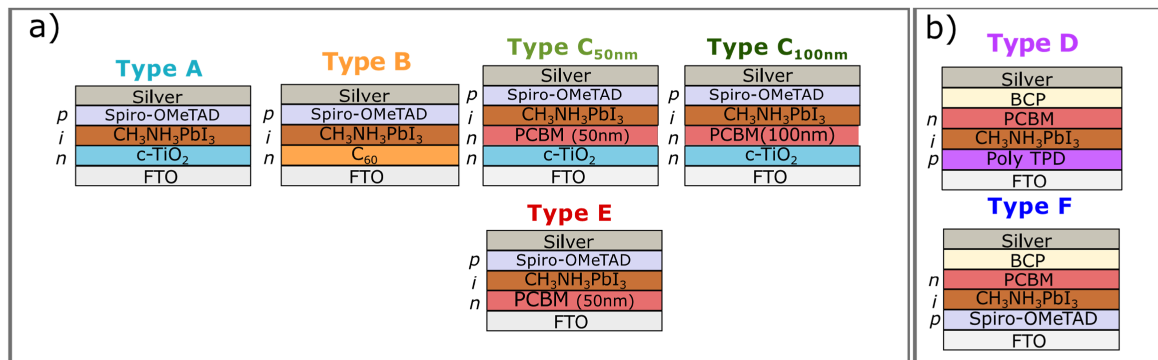

Figure S1. **a)** The whole series of normal type devices structures studied **b)** The series of inverted type device structures studied.

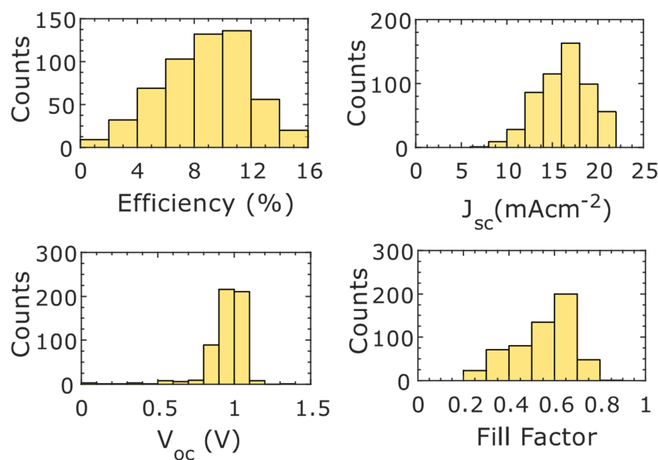

Figure S1. **c)** Histograms showing the combined statistics for the reverse sweep device parameters (current density (J_{sc}), Power conversion efficiency, Fill Factor and Open Circuit Voltage (V_{oc})) for all device architectures types A-F shown in Figure S1a and b.

Device characteristics Relating to Figure 1

	PCE (%)	J_{sc} ($mAcm^{-2}$)	V_{oc} (V)	FF	SPO (%)	SJ ($mAcm^{-2}$)
Type A	15.8	20.2	1.04	0.75	1.8	2.2
Type B	15.4	21.3	1.07	0.68	15.0	18.0
Type C	13.6	20.6	1.10	0.61	13.6	17.1
Type D	12.9	17.3	1.06	0.72	14.1	16.0

Table S1. A table showing the power conversion efficiencies (PCE), short circuit current density(J_{sc}), open circuit voltage (V_{oc}), fill factor (FF), stabilized power conversion efficiency (SPCE), stabilized current density (SJ) derived from the reverse JV sweeps of champion devices presented in Figure 1a.

Comparison of Type B (regular) and Type D (inverted) device

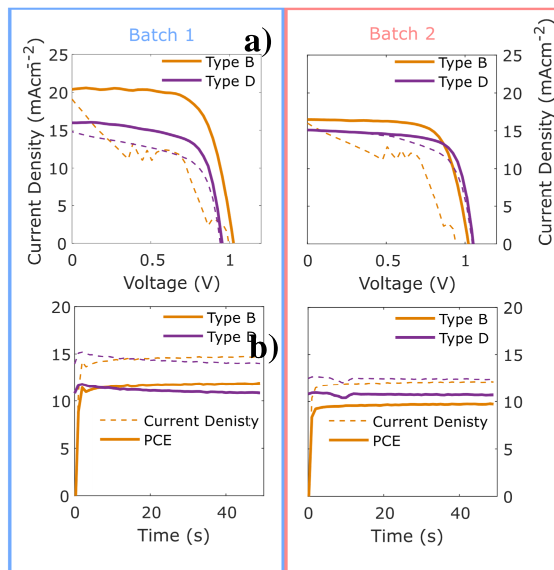

Figure S2. a) Current voltage characteristics to show the hysteresis on Type B and D devices grown in the in the same batch. The dashed lines represent the forward sweep from J_{sc} to V_{oc} **b)** The stabilised PCE and current density of the two types of devices.

The stabilisation efficiencies are similar even though type B device shown much more hysteresis. This indicates that a representative SPO of the PCE can be achieve in both inverted and regular device architectures. The hysteresis is due to pinholes observed in the C_{60} layer as observed in the SEM in figure S8.

Using Spiro-OMeTAD in an inverted device (Type F)

c)

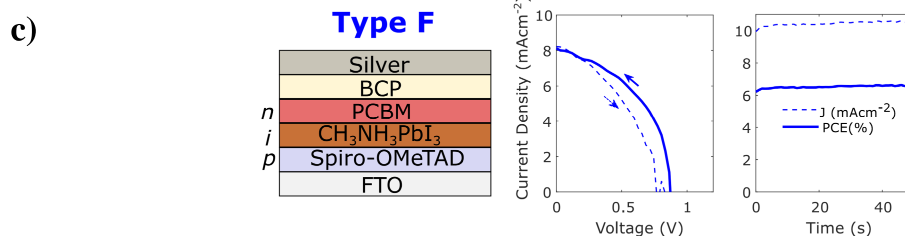

Figure S2 c) Current voltage curves for the device with the structure shown. Here the device is in an inverted configuration with the hole transport layer is changed from Poly-TPD to Spiro-OMeTAD. Type D and Type F (figure S2c) are devices which have the same architecture and ETL (PCBM) but differing HTLs, yet they both show relatively high SPO's

in comparison to Type A devices. Type F incorporates Spiro-OMeTAD as its HTL, and the SPO is representative of the PCE. This implies that in Type A devices, the source of the low SPO originates from the TiO2 layer in the device. The slight hysteresis observed may be due to pinholes in the Spiro OMeTAD film.

Transmission Electron Microscopy

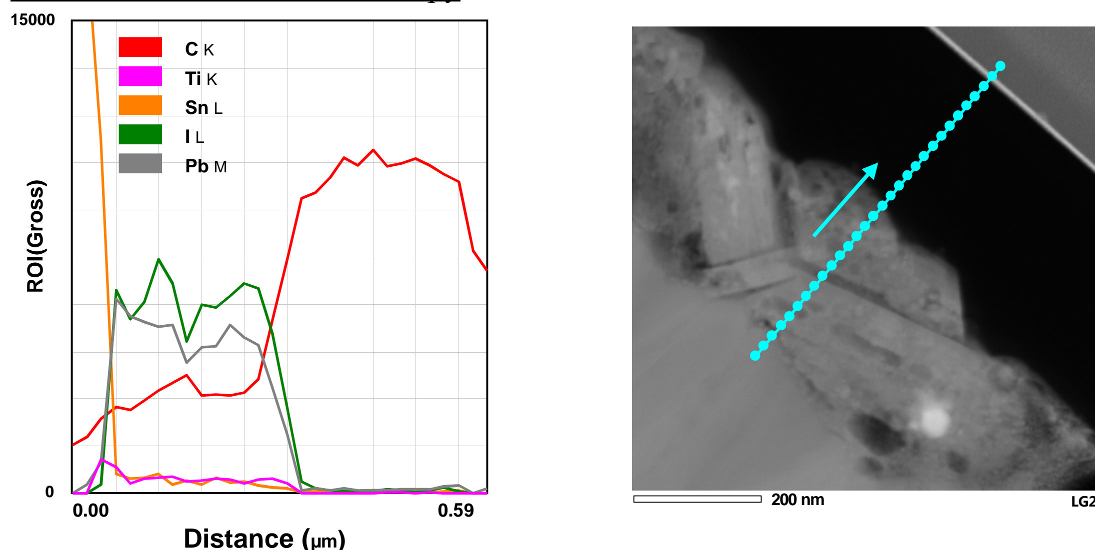

Figure S3 a) Plot showing the integrated counts for the ROI of different elements in a line scan performed on sample Y, showing presence of Ti from TiO_2. **b)** corresponding HAADF image showing the linescan and its direction.

An EDS linescan was carried out across the device structure of the TEM sample Y and at each point, individual spectra were collected from point analyses. The counts within the region of interest (ROI) related to the EDS peaks of the different elements were integrated at each analysis point and are plotted as a function of distance along the linescan direction. The Ti Kα line (4.507 eV) overlaps closely with the I $L\beta^2$ line (4.506 eV). The plot in Figure S3a shows the detection of Ti in the TiO_2 layer by EDS with a peak in the ROI counts for the Ti K line at the interface between the FTO and the $MAPbI_3$ at the point where the Sn L signal dips while the I L signal rises. The constant Ti Kα signal within the $MAPbI_3$ layer is an artifact due to the strong overlapping I $L\beta^2$ signal in the $MAPbI_3$ layer.

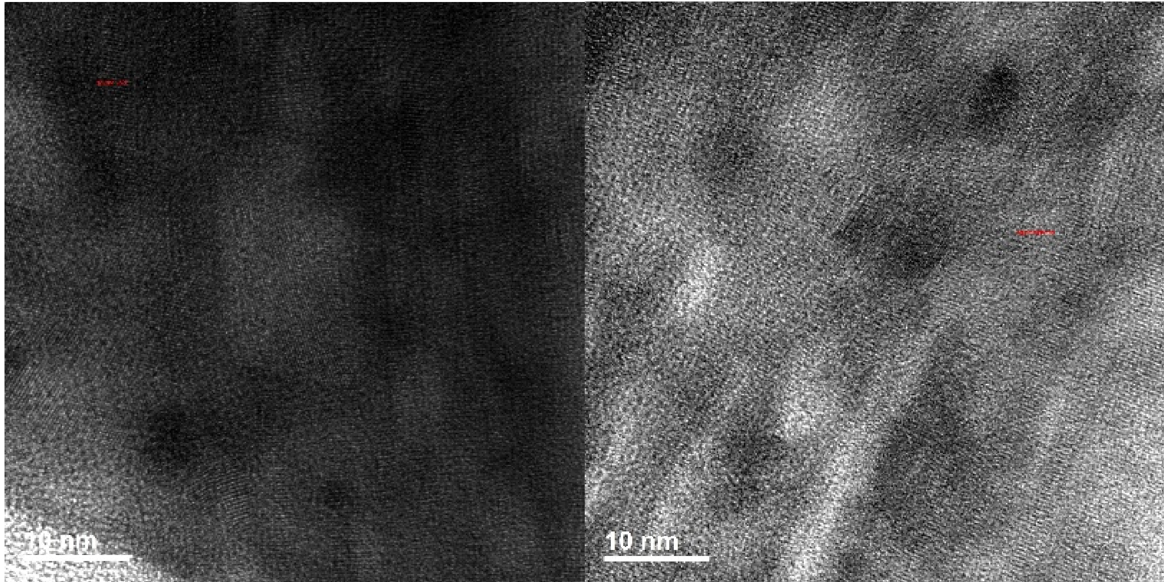

Figure S3 c) HRTEM micrograph of sample Z showing the nanovoids

We note that nanosized faceted voids were also observed in perovskite crystals in both types of devices.

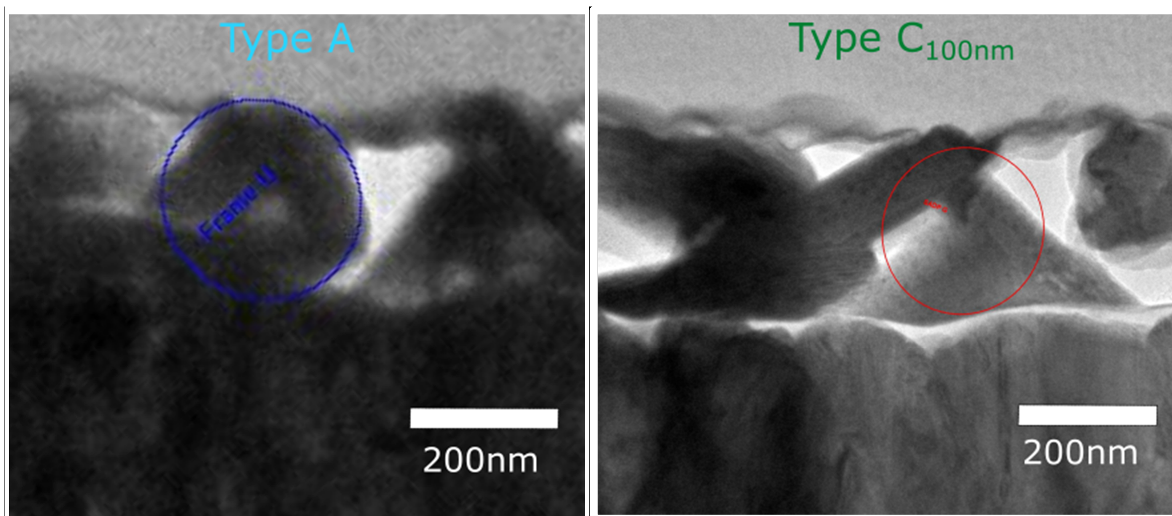

Figure S3 d) Shows the area characterised and looked in more detail by HRTEM, HAADF , EDX and Electron diffraction analysis in figure 3.

Thermal Admittance Spectroscopy & Photoluminescence Transient plots

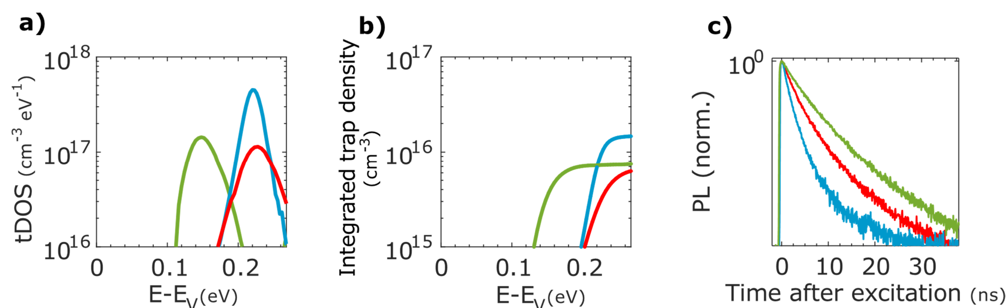

Figure S4. a) The trap density of states (tDOS) for type A (blue line), type C_{50nm} (green line) and type E (red line) $MAPbI_3$ photovoltaic devices. **b**) The integrated trap density for the $MAPbI_3$ when contacted to the n-types layers calculated by integrating the individual curves. **c)** Photoluminescence transients for thin films of c-TiO_2/$MAPbI_3$ (blue line) representing the type A device architecture, c-TiO_2/PCBM/$MAPbI_3$ (green line) representing the type 50_{nm} device architecture and PCBM/$MAPbI_3$ (red line) representing the type E device architecture.

The integrated trap state density of the $MAPbI_3$, calculated by integrating the tDOS curve from Figure 3a, was 1.46×10^{16} cm^{-3} for the device containing only c-TiO_2 as the ETL (type A). In contrast for device with only PCBM (type E), the tDOS is lower at 0.66×10^{16} cm^{-3}. The trap depth with c-TiO_2 only devices is 0.22 eV and noticeably, the trap depth for $MAPbI_3$ in devices with only PCBM(Type-E) is similarly deep. The deeper traps in the $MAPbI_3$ in type E devices suggests that due to the pinholes observed in the PCBM (figure 2d), the resulting FTO/$MAPbI_3$ interface encompasses even more defects, than a c-TiO_2/$MAPbI_3$ interface. This may explain the hysteresis observed in the type E device. The insertion of PCBM, in combination with c-TiO_2 shows a reduced trap density in the $MAPbI_3$ perovskite. In contrast, for the device with only PCBM (type E), the tDOS is lower at 0.66×10^{16} cm^{-3}. The device with dual-ETL (type C_{50nm} and C_{100nm}) benefits from this effect of PCBM, whilst the c-TiO_2 prevents the direct contact of the FTO/$MAPbI_3$. This is further

reflected in the photoluminescence (PL) transient (Figure S4) showing a longer carrier lifetime in case PCBM is present. The interface consisting of only c-TiO_2 quenches the PL most. c-TiO_2 has been previously shown to be an inefficient electron extractor, from both the device performances in Figure 2a and in previous experiments,[30,41] it can be concluded that the PL lifetime is short, not due to charge extraction but due to the high trap density which results in an increased non-radiative recombination of charge carriers. Having dual-ETL interfacing the $MAPbI_3$ (green line), proves to have the longest lifetime.

	PCE [%]	**J_{sc} [mAcm^{-2}]**	**V_{oc} [V]**	**FF**	**SPO [%]**	**SJ [mAcm^{-2}]**
Type A	10.0 *(8.4)*	18.0 *(16.8)*	1.07 *(1.06)*	0.52 *(0.47)*	2.7 *(2.4)*	3.7 *(3.5)*
Type C_{50nm}	12.8 *(11.6)*	18.6 *(17.9)*	1.07 *(1.07)*	0.65 *(0.61)*	12.4 *(11.8)*	15.4 *(14.6)*
Type C_{100nm}	10.2 *(8.5)*	13.7 *(13.1)*	1.07 *(1.04)*	0.68 *(0.62)*	9.7 *(9.2)*	11.2 *(11.1)*
Type E	12.4 *(11.6)*	19.4 *(18.3)*	1.07 *(1.07)*	0.60 *(0.59)*	10.9 *(11.0)*	14.6 *(13.4)*

Device characteristics Relating to Figure 3.

Table S2 Showing the devices performance of the devices shown in Figure 2. Where the numbers in the brackets represent a mean average of at least 6 devices from the batch in study.

External Quantum Efficiency Measurements.

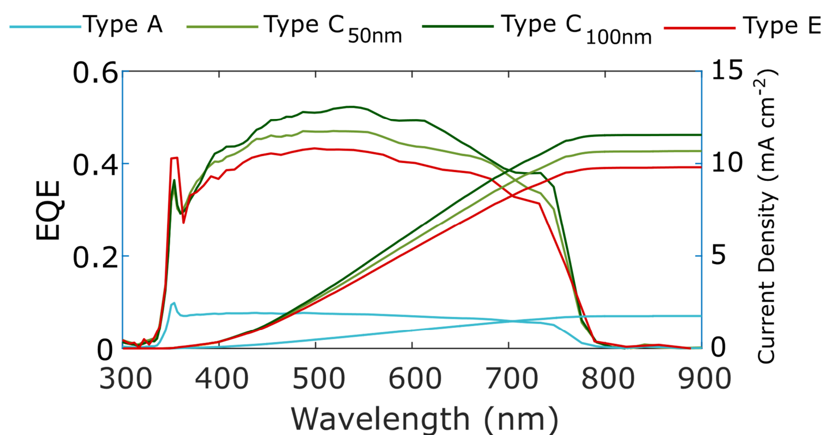

Figure S5. The EQE spectra with the cumulative photogenerated current at each wavelength using the ASTM G173-03 Global Tilt reference spectrum of the devices exhibited in **Figure 2** and **Table S2.**

Thermal admittance spectroscopy (TAS): Morr-Schottky Plots

Mott-Schottky plots:

Measured capacitance at 10kHz vs. Bias voltage at 294 K.

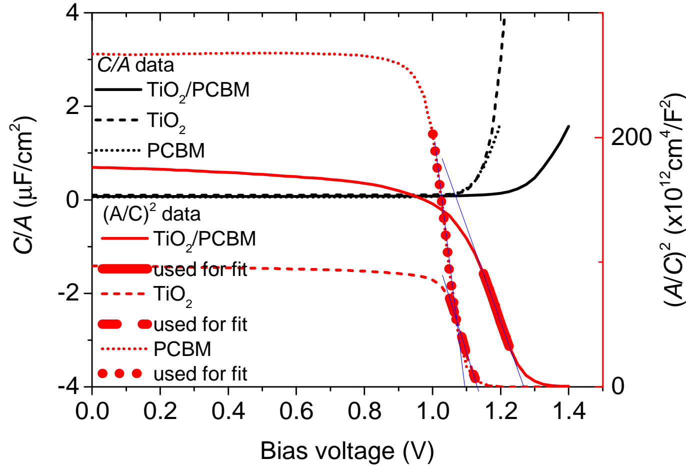

Figure S6 Mott-Schottky plots for perovskite solar cells with n-type contact layers comprising TiO_2/PCBM, TiO_2, and PCBM. The blue lines are extrapolations to determine the built-in voltage.

From extrapolating $(A/C)^2$ graphs to A/C=0 follows the built in voltage (see table). The slope of the extrapolation can be used to determine the doping density N_d (e.g. due to traps) and the depletion width W (see table) at $V_{bias} = 0$ V:

$$N_d = -\frac{2}{q\varepsilon}\left(\frac{d(C/A)^{-2}}{dV}\right)^{-1},$$

$$w = \sqrt{\frac{2\varepsilon(V_{bi}-V_{bias})}{qN_d}},$$

Where ε is the dielectric constant (ε_r for this perovskite is 30)[38]

Temperature dependence of the frequency dependent capacitance is shown in Figure S7a, b and c for all 3 types of cells. Steps are observed in these spectra that shift to lower frequency for lower temperature. The transition frequency can be related to the rate of carrier emission and capture from traps in the bandgap.[38] We assume that the occupancy of these states is in thermal equilibrium and hence is determined by the Fermi-Dirac

distribution. Therefore, the trap energy E_a and the characteristic transition frequency ω_0 can be expressed as:

$$\omega_0 = 2DT^2 exp\left(-\frac{E_a}{kT}\right), \qquad 3$$

Where D is a constant related to the effective density of states in the conduction band, the thermal velocity and the carrier capture cross-section.[42–44]

dC/df plots extracted from Figure S7 a,b, and c, can be used to determine the frequency that relates to the temperature dependent shift of the steps observed at the high frequency regions in Figure S7 a, b and c. This frequency is plotted in Figure S7d, e, and f as a function of temperature.

Now the activation energy of the trap states can be determined from Figure S7d, e, and f in combination with Eq.3. The activation energy of the traps was found to be roughly 0.15 eV for cells with TiO_2/PCBM, 0.22 eV for cells with TiO2, and 0.22 eV for cells with PCBM.

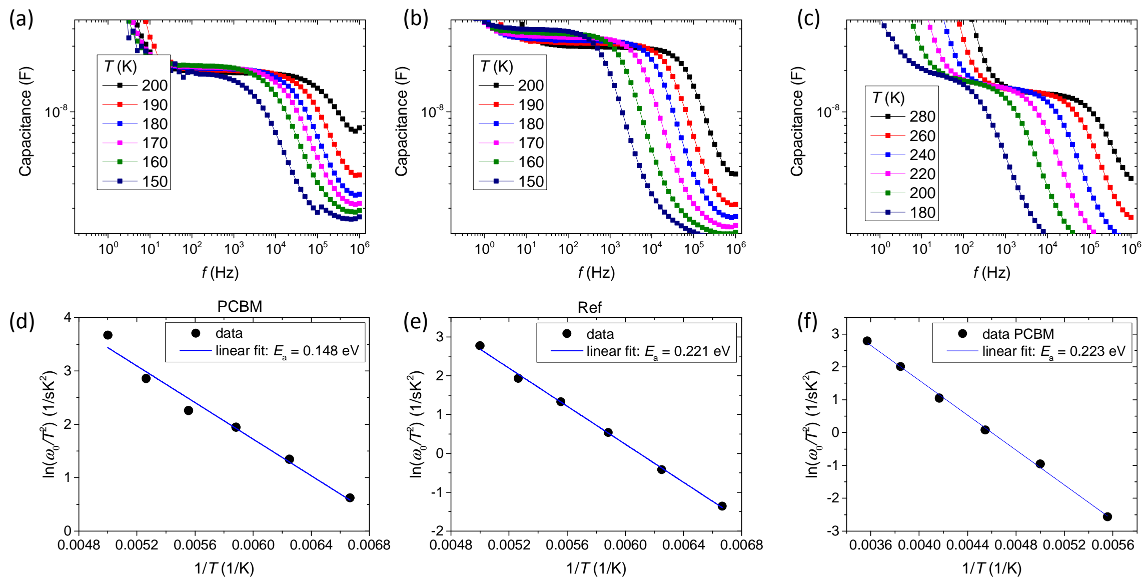

Figure S7 Temperature dependence of capacitance for perovskite solar cells with n-type contact layers comprising **a)** TiO_2/PCBM, **b)** TiO_2, and **c)** PCBM. Arrhenius plots of the characteristic frequencies to extract the defect activation energy for perovskite solar cells with n-type contact layers comprising **d)** TiO_2/PCBM, **e)** TiO_2, and **f)** PCBM.

Now the frequency dependent capacitance can be used to determine the energetic profile of the tDOS:

$$N_t = \frac{V_{bi}}{qW}\frac{dC}{d\omega}\frac{\omega}{kT}.$$

Scanning electron microscopy images of the various device architectures studied.

a) Type A

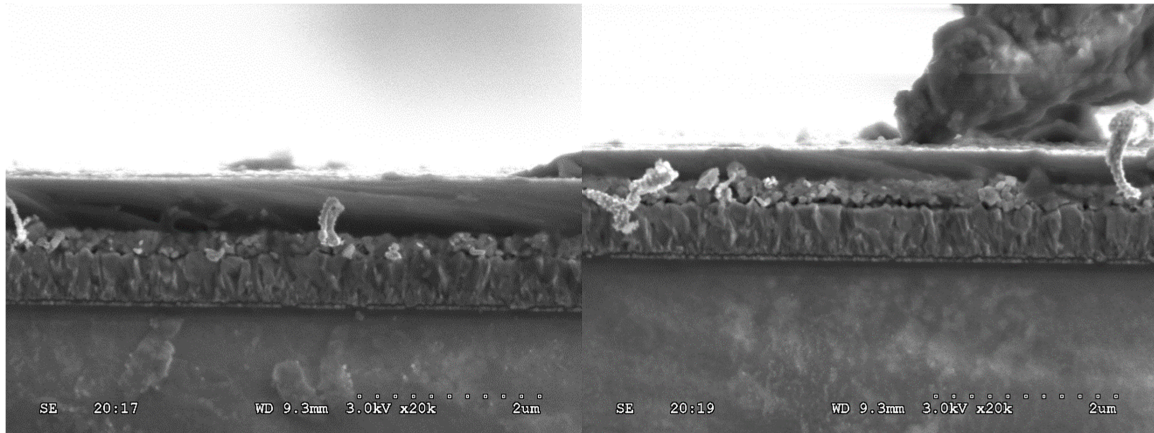

b) Type B

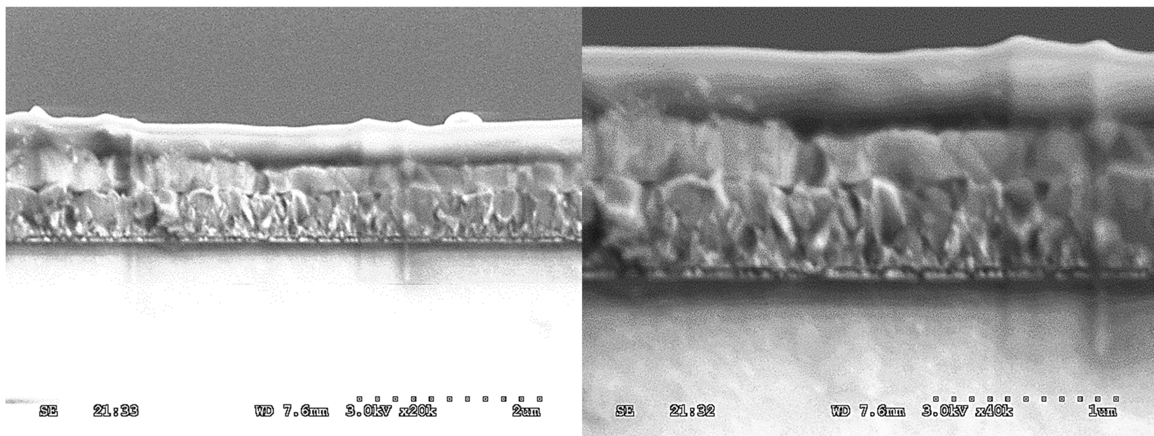

c) Type C_{50nm}

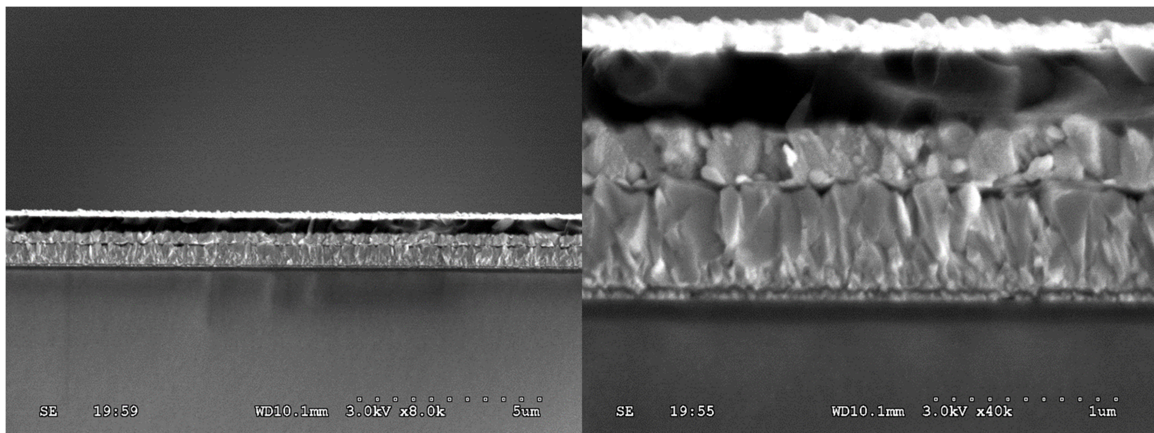

d) Type C_{100nm}

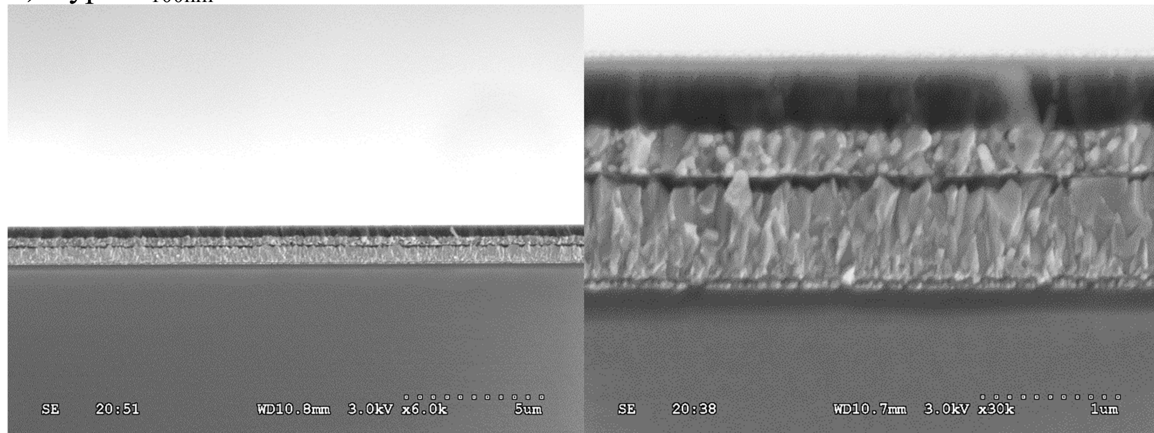

e) Type E

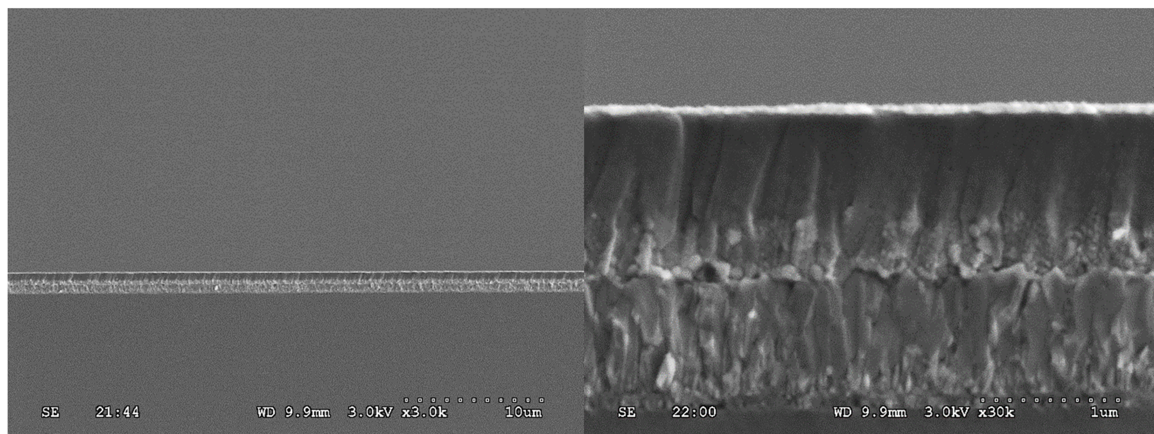

Figure S8. Showing various magnifications of the different device structures. Where **a)** Type A **b)** Type B **c)** Type C_{50nm} **d)** type C_{100nm} **e)** Type E

Absorbance spectra.

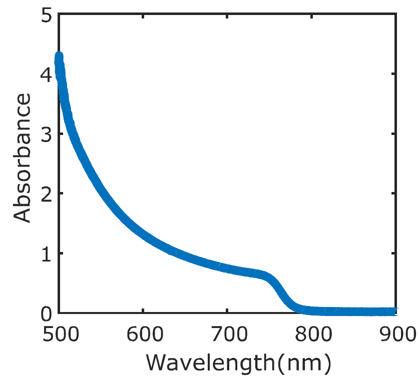

Figure S9. The Absorbance spectra for the evaporated films on z-cut quartz

X-ray Diffraction Pattern.

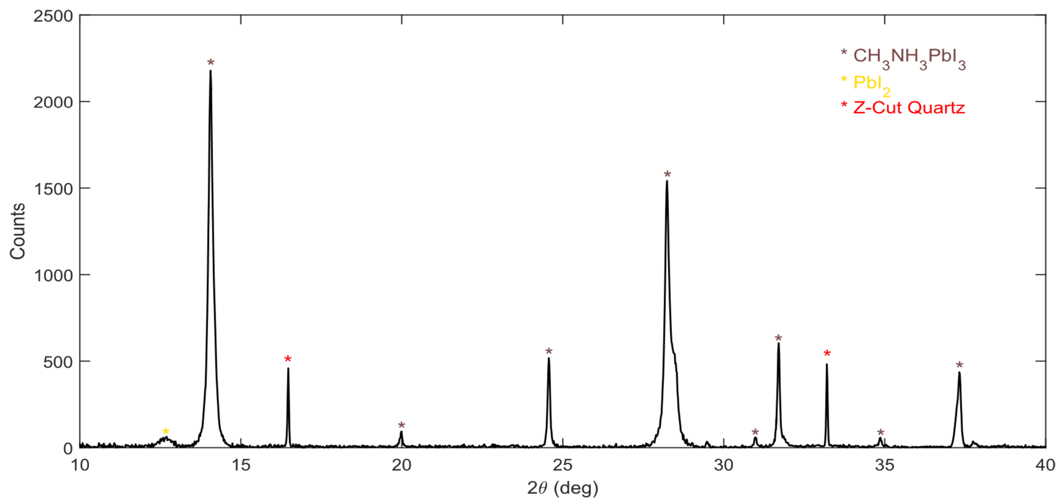

Figure S10. The X-ray diffraction pattern for the thermally evaporated $MAPbI_3$ grown on quartz.

Equation S1

Fill Factor (FF) and Power Conversion Efficiency(PCE)

$$PCE = \frac{V_{oc} J_{sc} FF}{p_{in}} \qquad where\ FF = \frac{V_{mp} J_{mp}}{V_{oc} J_{sc}}$$

Where V_{oc} is the open circuit voltage, J_{sc} is the short circuit current density, V_{mp} is the voltage at maximum power point, J_{mp} is the current density at the maximum power point, P_{in} is the incident light power.

References

[1] National Renewable Energy Laboratory, "National Center for Photovoltaics," can be found under http://www.nrel.gov/ncpv/, **2016**.

[2] H. J. Snaith, A. Abate, J. M. Ball, G. E. Eperon, T. Leijtens, N. K. Noel, S. D. Stranks, J. T.-W. Wang, K. Wojciechowski, W. Zhang, *J. Phys. Chem. Lett.* **2014**, *5*, 1511.

[3] Y. Zhang, M. Liu, G. E. Eperon, T. C. Leijtens, D. McMeekin, M. Saliba, W. Zhang, M. de Bastiani, A. Petrozza, L. M. Herz, M. B. Johnston, H. Lin, H. J. Snaith, *Mater. Horiz.* **2015**, *2*, 315.

[4] N. J. Jeon, J. H. Noh, W. S. Yang, Y. C. Kim, S. Ryu, J. Seo, S. Il Seok, *Nature* **2015**, *517*, 476.

[5] H.-S. Kim, N.-G. Park, *J. Phys. Chem. Lett.* **2014**, *5*, 2927.

[6] S. van Reenen, M. Kemerink, H. J. Snaith, *J. Phys. Chem. Lett.* **2015**, *6*, 3808.

[7] W. Tress, N. Marinova, T. Moehl, S. M. Zakeeruddin, M. K. Nazeeruddin, M. Grätzel, *Energy Environ. Sci.* **2015**, *8*, 995.

[8] Y. Yuan, J. Huang, *Acc. Chem. Res.* **2016**, *49*, 286.

[9] M. M. Lee, J. Teuscher, T. Miyasaka, T. N. Murakami, H. J. Snaith, *Science* **2012**, *338*, 643.

[10] S. D. Stranks, G. E. Eperon, G. Grancini, C. Menelaou, M. J. P. Alcocer, T. Leijtens, L. M. Herz, A. Petrozza, H. J. Snaith, *Science* **2013**, *342*, 341.

[11] C. Wehrenfennig, G. E. Eperon, M. B. Johnston, H. J. Snaith, L. M. Herz, *Adv. Mater.* **2014**, *26*, 1584.

[12] R. L. Milot, G. E. Eperon, H. J. Snaith, M. B. Johnston, L. M. Herz, *Adv. Funct. Mater.* **2015**, *25*, 6218.

[13] M. B. Johnston, L. M. Herz, *Acc. Chem. Res.* **2016**, *49*, 146.

[14] W. Zhang, M. Saliba, D. T. Moore, S. K. Pathak, M. T. Hörantner, T. Stergiopoulos, S. D. Stranks, G. E. Eperon, J. A. Alexander-Webber, A. Abate, A. Sadhanala, S. Yao, Y.

Chen, R. H. Friend, L. A. Estroff, U. Wiesner, H. J. Snaith, *Nat. Commun.* **2015**, *6*, 6142.

[15] D. B. Mitzi, M. T. Prikas, K. Chondroudis, *Chem. Mater.* **1999**, *11*, 542.

[16] S. D. Stranks, S. M. Wood, K. Wojciechowski, F. Deschler, M. Saliba, H. Khandelwal, J. B. Patel, S. J. Elston, L. M. Herz, M. B. Johnston, A. P. H. J. Schenning, M. G. Debije, M. K. Riede, S. M. Morris, H. J. Snaith, *Nano Lett.* **2015**, *15*, 4935.

[17] J. B. Patel, R. L. Milot, A. D. Wright, L. M. Herz, M. B. Johnston, *J. Phys. Chem. Lett.* **2016**, *7*, 96.

[18] M. Saliba, T. Matsui, J.-Y. Seo, K. Domanski, J.-P. Correa-Baena, M. K. Nazeeruddin, S. M. Zakeeruddin, W. Tress, A. Abate, A. Hagfeldt, M. Grätzel, *Energy Environ. Sci.* **2016**, *9*, 1989.

[19] Q. Lin, A. Armin, R. C. R. Nagiri, P. L. Burn, P. Meredith, *Nat. Photonics* **2014**, *9*, 106.

[20] M. Liu, M. B. Johnston, H. J. Snaith, *Nature* **2013**, *501*, 395.

[21] D. P. McMeekin, G. Sadoughi, W. Rehman, G. E. Eperon, M. Saliba, M. T. Horantner, A. Haghighirad, N. Sakai, L. Korte, B. Rech, M. B. Johnston, L. M. Herz, H. J. Snaith, *Science* **2016**, *351*, 151.

[22] W. S. Yang, J. H. Noh, N. J. Jeon, Y. C. Kim, S. Ryu, J. Seo, S. Il Seok, *Science* **2015**, *348*, 1234.

[23] M. Era, T. Hattori, T. Taira, T. Tsutsui, *Chem. Mater.* **1997**, *9*, 8.

[24] D. M. Mattox, *Handbook of Physical Vapor Deposition (PVD) Processing*, William Andrew, **2010**.

[25] M. A. Pérez-Osorio, R. L. Milot, M. R. Filip, J. B. Patel, L. M. Herz, M. B. Johnston, F. Giustino, *J. Phys. Chem. C* **2015**, *119*, 25703.

[26] W. Zhang, G. E. Eperon, H. J. Snaith, *Nat. Energy* **2016**, *1*, 16048.

[27] J. T.-W. Wang, Z. Wang, S. Pathak, W. Zhang, D. W. DeQuilettes, F. Wisnivesky-Rocca-Rivarola, J. Huang, P. K. Nayak, J. B. Patel, H. A. Mohd Yusof, Y. Vaynzof, R.

Zhu, I. Ramirez, J. Zhang, C. Ducati, C. Grovenor, M. B. Johnston, D. S. Ginger, R. J. Nicholas, H. J. Snaith, *Energy Environ. Sci.* **2016**, *9*, 2892.

[28] Editorial, *Nat. Photonics* **2015**, *9*, 703.

[29] P. V. Kamat, *J. Phys. Chem. C* **2012**, *116*, 11849.

[30] K. Wojciechowski, T. Leijtens, S. Siprova, C. Schlueter, M. T. Hörantner, J. T.-W. Wang, C.-Z. Li, A. K.-Y. Jen, T.-L. Lee, H. J. Snaith, *J. Phys. Chem. Lett.* **2015**, *6*, 2399.

[31] R. S. Ruoff, D. S. Tse, R. Malhotra, D. C. Lorents, *J. Phys. Chem.* **1993**, *97*, 3379.

[32] L. Cojocaru, S. Uchida, P. V. V. Jayaweera, S. Kaneko, J. Nakazaki, T. Kubo, H. Segawa, *Chem. Lett.* **2015**, *44*, 1750.

[33] C. Tao, S. Neutzner, L. Colella, S. Marras, A. R. Srimath Kandada, M. Gandini, M. de Bastiani, G. Pace, L. Manna, M. Caironi, C. Bertarelli, A. Petrozza, *Energy Environ. Sci.* **2015**, *8*, 2365.

[34] G. Richardson, S. E. J. O'Kane, R. G. Niemann, T. A. Peltola, J. M. Foster, P. J. Cameron, A. B. Walker, *Energy Environ. Sci.* **2016**, DOI 10.1039/C5EE02740C.

[35] J. Xu, A. Buin, A. H. Ip, W. Li, O. Voznyy, R. Comin, M. Yuan, S. Jeon, Z. Ning, J. J. McDowell, P. Kanjanaboos, J.-P. Sun, X. Lan, L. N. Quan, D. H. Kim, I. G. Hill, P. Maksymovych, E. H. Sargent, *Nat. Commun.* **2015**, *6*, 7081.

[36] N. Sakai, S. Pathak, H.-W. Chen, A. A. Haghighirad, S. D. Stranks, T. Miyasaka, H. J. Snaith, *J. Mater. Chem. A* **2016**, *4*, 4464.

[37] Y. Shao, Z. Xiao, C. Bi, Y. Yuan, J. Huang, *Nat. Commun.* **2014**, *5*, 5784.

[38] H.-S. Duan, H. Zhou, Q. Chen, P. Sun, S. Luo, T.-B. Song, B. Bob, Y. Yang, *Phys. Chem. Chem. Phys.* **2015**, *17*, 112.

[39] L. A. Giannuzzi, F. A. Stevie, *Micron* **1999**, *30*, 197.

[40] B. W. Kempshall, L. A. Giannuzzi, B. I. Prenitzer, F. A. Stevie, S. X. Da, *J. Vac. Sci. Technol. B Microelectron. Nanom. Struct.* **2002**, *20*, 286.

[41] G. Xing, B. Wu, S. Chen, J. Chua, N. Yantara, S. Mhaisalkar, N. Mathews, T. C. Sum, *Small* **2015**, *11*, 3606.

[42] V. Gonzalez-Pedro, E. J. Juarez-Perez, W.-S. Arsyad, E. M. Barea, F. Fabregat-Santiago, I. Mora-Sero, J. Bisquert, *Nano Lett.* **2014**, *14*, 888.

[43] a. Poglitsch, D. Weber, *J. Chem. Phys.* **1987**, *87*, 6373.

[44] A. Jasenek, U. Rau, V. Nadenau, H. W. Schock, *J. Appl. Phys.* **2000**, *87*, 594.